WELDING RESEARCH

SUPPLEMENT TO THE WELDING JOURNAL, SEPTEMBER, 1981
Sponsored by the American Welding Society and the Welding Research Council

Hydrogen-Assisted Cracking in HSLA Pipeline Steels

A major finding of research sponsored by AISI and guided by WRC is that close correlation is obtained between the widely used implant test and the slot weld test recently developed as a simple, reliable and convenient method for assessing the field weldability of pipeline steels

BY R. VASUDEVAN, R. D. STOUT AND A. W. PENSE

ABSTRACT. Hydrogen-assisted cracking susceptibilities of three heats of high-strength low alloy pipeline steels were studied using the newly developed slot weldability test as well as the implant test. The aims were:

1. To compare the slot weld test with a weldability test already in wide use such as the implant test.
2. To gain a better understanding of the initiation, kinetics and morphology of hydrogen-assisted cracking in high-strength pipeline steels, with particular reference to low carbon microalloyed steel by fractography and acoustic emission monitoring techniques.

Correlation studies showed that the critical stresses for cracking for the heats of steel studied were in the same order as their susceptibilities to cold cracking in slot weldability tests.

Acoustic emission and fractographic studies conducted on implant as well as slot weldability tests indicated the following in a straight 0.26% carbon-manganese steel:

1. Crack initiation occurred immediately after loading at all hydrogen levels examined.
2. Crack growth occurred during the entire test by relatively fast quasi-cleavage and microvoid coalescence processes with little contribution from intergranular processes.

By contrast, in a low carbon microalloyed steel, crack initiation occurred immediately after loading at high hydrogen levels for all stress levels examined. Also, a definite incubation period was noted at lower stress levels when welded with low hydrogen electrodes. The lower the stress, the longer was the incubation period. The morphology of crack growth in the microalloyed steel was predominantly intergranular (a relatively slow process as indicated by acoustic emission studies) at low stress intensities, giving way, progressively, to quasi-cleavage and microvoid coalescence with increasing stress intensity. Both the morphology and kinetics of crack growth were shown to be strongly influenced by the microstructure.

The changes observed in both fracture mode and crack growth rates in the materials studied in this investigation were compatible with the hydrogen-assisted cracking model proposed by Beachem (Ref. 19) and by the lattice decohesion theory.

Paper presented at the 62nd AWS Annual Meeting held in Cleveland, Ohio, during April 5-10, 1981.

R. VASUDEVAN, formerly a Research Assistant at Lehigh University, is with the Linde Division, Union Carbide Corporation, Ashtabula, Ohio; R. D. STOUT is Dean Emeritus of the Graduate School, and A. W. PENSE is Chairman, Department of Metallurgy and Materials Engineering, Lehigh University, Bethlehem, Pennsylvania.

Introduction

In the construction of pipelines by the "stove pipe" technique, girth welding is often accomplished under difficult conditions of weather and terrain. Further, the combination of high hydrogen potential cellulosic electrodes for the root pass, low heat inputs in the interest of speed, and the relatively high carbon equivalents of many traditional high-strength pipeline steels (higher carbon content) have enhanced the potential of hydrogen-induced cracking, a matter of great concern to the constructor. This has led to the development of low carbon microalloyed steels combining high strength and excellent toughness with a markedly reduced susceptibility to hydrogen-induced cracking. The increased resistance to hydrogen-

Table 1.—Composition of Pipeline Steels, Wt-%

Heat	Pipe dimensions, mm Diameter	Wall	C	Mn	P	S	Si	Ni	Mo	Cb	V	Al
492S1871	1050	14.6	0.26	1.36	0.011	0.025	0.04	—	—	0.031	0.06	—
C10113	1200	18.3	0.05	2.04	0.010	0.006	0.29	0.25	0.58	0.06	—	0.04
B259	900	15.7	0.08	1.15	0.020	0.004	0.23	—	—	0.05	—	—

Table 2.—Mechanical Properties of Pipeline Steels

Heat	Yield strength, MPa[a]	Tensile strength, MPa[a]	Elongation in 50 mm, %
492S1871	547.4	688.1	25
C10113	574.3	772.2	39
B259	448.2	507.5	42

[a]MPa ÷ 6.895 = ksi

Table 3—Hydrogen-Assisted Cracking Results With Slot Weld Test Specimen (Ref. 1)[a],[b]

	Heat 492S1871	C10113	B259	
C.E.[c]	0.50	0.52	0.27	
% cracking (with HYP E7010) after elapsed times of:	24 h	80	25	Nil
	20 min	50	5	
	10 min	50	—	
	5 min	40	3	
	1 min	10	—	
Coarse grained HAZ hardness—1 kg load, DPH	360	340		

[a]Welding conditions: current—150 A; travel speed—30 cm/min; H.I.—9 kJ/cm; preheat—20°C.
[b]None of the steel heats exhibited cracking when welded with E7018 electrode.
[c]C.E. (IIW) = C ÷ Mn/6 + (Cr + Mo + V)/5 + Ni + Cu)/15

induced cracking of low carbon microalloyed steels, compared to that of straight C-Mn steel of the same carbon equivalent (IIW formula), was demonstrated recently by the slot weld test (Ref. 1).

The critical hydrogen concentration necessary for cracking to occur is a function of both the stress and the microstructure. The most definitive characteristic of hydrogen-assisted cracking (HAC) is the existence of a lower critical stress (applied or residual) below which HAC will not occur.

Susceptibility to HAC, as mentioned above, is also dependent on the microstructure of the steel. It is now generally accepted that twinned martensite exhibits greater susceptibility to HAC than slipped martensite (Ref. 2, 3). Bainites, which form as sheaves of narrow, parallel ferrite laths, have an intermediate susceptibility to hydrogen cracking. Slipped martensite, autotempered low carbon martensite and granular bainite are least embrittled (Ref. 2-4). Small amounts of twinning in slipped martensite increase the index of embrittlement considerably (Ref. 2). Larger prior austenite grain size also increases embrittlement (Ref. 2) as the size of both martensite crystals and bainitic colonies is enlarged. Fractographic analyses by Boniszewski (Ref. 2-4) and others (Ref. 5-7) tend to support the observation that hydrogen embrittlement in steel does not result in cracking of a specific morphology; instead, it exploits the easiest crack nucleation mechanism in a given microstructure.

Weldability Tests

Since hydrogen-induced cracking is so important to weldability, there has been a proliferation of tests proposed to evaluate this tendency. All the weldability tests can be broadly classified into two groups:

1. Self-restraint tests (such as the Lehigh test, the bead-on-plate test, and the Y-groove tekken test*).
2. The external restraint tests (such as RRC test and implant test).

A drawback of these weldability tests is that all utilize elaborate laboratory techniques including metallography to study the extent of cracking in steels; hence, they are unsuitable to field pipe fabrication conditions. Moreover, some do not match welding conditions used on pipe construction, and others lack the unique configuration of pipes.

The slot weld test (Ref. 1) was developed to be a simple, reliable, and a more convenient test for assessing the field weldability of pipeline steels. Also, the variety of weldability tests (Ref. 8-12) make it desirable to correlate the various weldability tests for a better understanding of the individual tests. Hence, it was decided to correlate the slot weld test with a test already in wide use such as the implant test.

Theories of Hydrogen Cracking

The damaging effects of hydrogen in materials have been recognized and investigated for more than a century. Nonetheless, there is considerable controversy over the mechanism of initiation and kinetics of hydrogen-induced cracking. To date, basically five major theories have been proposed to explain the embrittling effects of hydrogen on the iron-iron bond:

1. The planar pressure theory of Zapffe and Sims (Ref. 13) modified by Tetelman (Ref. 14)
2. The surface adsorption theory of Petch and Stables (Ref. 15, 16)
3. The lattice interaction theory proposed by Troiano (Ref. 17)
4. The lattice decohesion theory advanced by Oriani (Ref. 18)
5. A mechanism based on modification of dislocation mobility proposed by Beachem (Ref. 19, 20)

Various other theories have been proposed, but they are essentially variations of the theories cited above. The evolution of these theories along with the controversy that still exists has been detailed previously (Ref. 20, 22). It seems that each of these theories is applicable to certain materials tested under specific conditions.

No single mechanism can explain all the experimental results to date. Nevertheless, in recent years, more credence is being given to hydrogen-assisted cracking, at least in high-strength steels. Recent studies in weld-

**Tekken test: Of Japanese origin—Y groove looks like a tilted Lehigh groove specimen.*

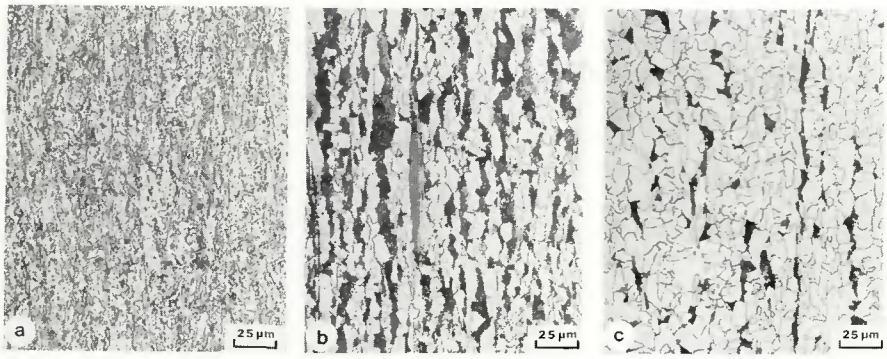

Fig. 1—Representative base metal microstructures: a—heat C10113; b—heat 492S1871; c—heat B259. Nital etch

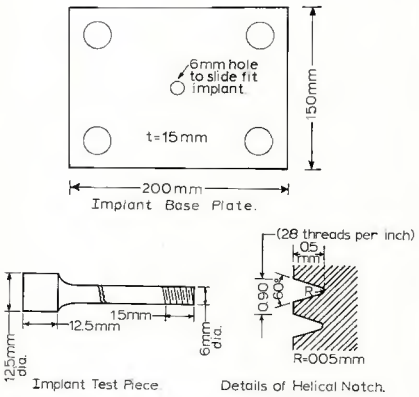

Fig. 2—Details of implant specimen and backing plate

ments (Ref. 21, 22) have supported such a model at the expense of the planar pressure theory.

Correlation of Implant and Slot Weld Tests

Materials Used

One of the objectives was to examine the correlation between the lower critical stress in the implant test (externally loaded testing method) with the extent of cracking obtained on the same heats of steel in the slot weld test (self-restraining specimen). For this reason steels with widely different cracking susceptibilities as evaluated by the slot weld test (Ref. 1) were selected for implant testing. They were heats 492S1871, B259 and C10113 (see Tables 1 and 2).

In earlier slot weldability tests (Table 3) when welded with HYP E7010 electrode, heat 492S1871 (0.26C-Mn steel) showed extensive cracking and B259 (0.08C-Mn steel) showed no cracking at all; on the other hand, C10113 (0.05C - microalloyed steel) showed moderate cracking even though its carbon equivalent was about the same as that of 492S1871. Representative microstructures of these heats of steel are given in Fig. 1.

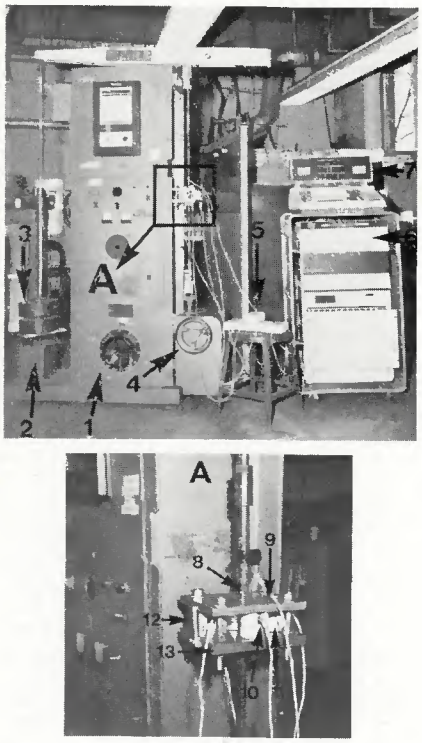

Fig. 3—Details of the implant testing machine and acoustic monitoring system. Overall (top): 1—implant testing M/C; 2—loading quill with microswitch; 3—load; 4—wheel for loading; 5—preamplifier; 6—AE system; 7—teleprinter. Inset A (bottom): 8—implant specimen; 9—implant base plate; 10—sensor; 11—magnet to hold sensor in position; 12—positioners for alignment; 13—backing plate

Experimental Procedure and Testing

The specimen design and testing procedure for conducting the slot weld test are given elsewhere (Ref. 23, 24). For implant testing, the implant design of Granjon (Ref. 25) modified (Ref. 26) with a helical notch to improve the reproducibility of the notch location with respect to the weld metal interface was employed.

The details of the base metal and implant are shown in Fig. 2. The base metal dimensions were chosen to match the dimensions of slot weld test specimens to keep the cooling rates in the two tests as close as possible. Since it was intended to compare different heats against each other by the implant test, a base metal thickness of 15 mm (19/32 in.) was chosen as a compromise.

The test was conducted using both high hydrogen (HYP E7010) and low hydrogen (E7018) electrodes. Test specimens were also welded by the GMA process using argon + 2% oxygen mixture at a flow rate of 1.42 m^3/h (50 cfh) as shielding gas to produce conditions where the only hydrogen encountered would be the residual hydrogen in the base metal, test piece and the welding wire electrode. For all the conditions the heat input was maintained at 9 kJ/cm (22 kJ/in.). E7010 electrodes were used in the as-received condition, whereas E7018 electrodes were baked at 370°C (698°F) and stored at 100°C (212°F) for at least 8 hours (h) before use. In the case of welding with E7018 electrodes, welding was performed 2 minutes (min) after taking the electrodes out of the oven.

A dead-weight creep testing machine was modified to perform as an implant testing machine. Figure 3 shows the details of the testing equipment used. The machine was equipped with an automatic timer actuated at the instant of loading and stopped by a microswitch on the loading grill when the specimen failed.

Before welding, both the implant and base metal were thoroughly degreased using acetone. Two minutes after performing the weld, which is the

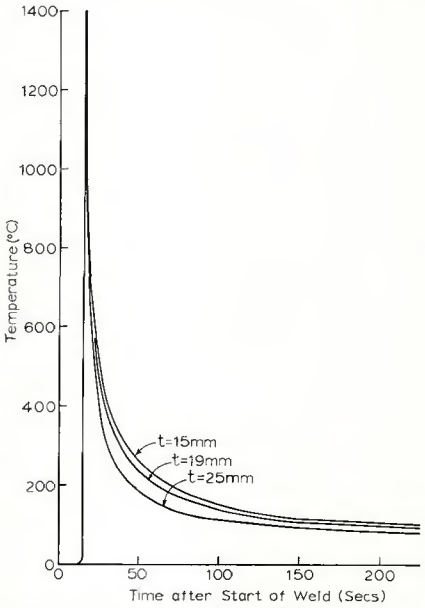

Fig. 4—Temperature-time profile at the center of the weld for various plate thicknesses (heat input = 9 kJ/cm)

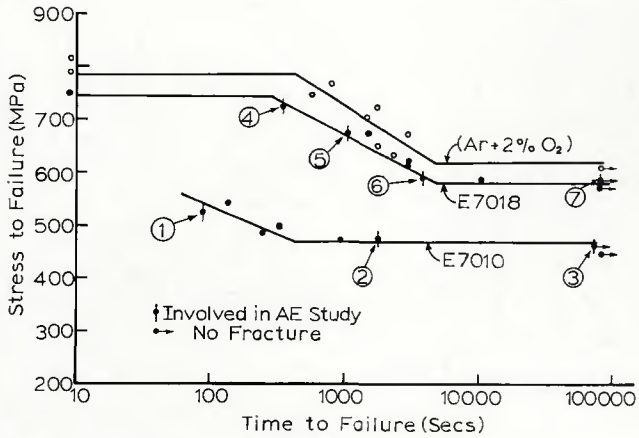

Fig. 5—Stress time-to-rupture curve for heat 492S1871

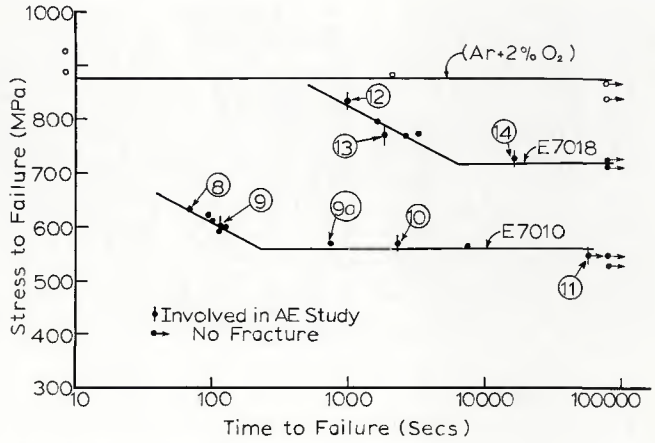

Fig. 6—Stress time-to-rupture curve for heat C10113

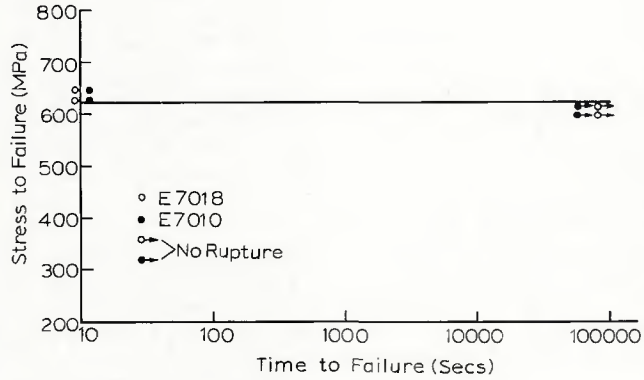

Fig. 7—Stress time-to-rupture curve for heat B259

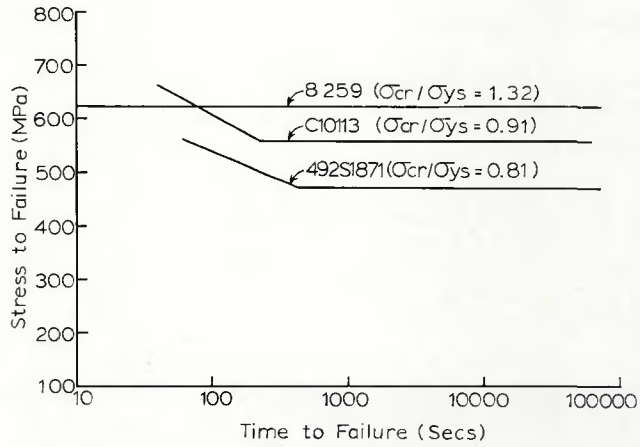

Fig. 8—Stress time-to-rupture curve for various heats welded with E7010

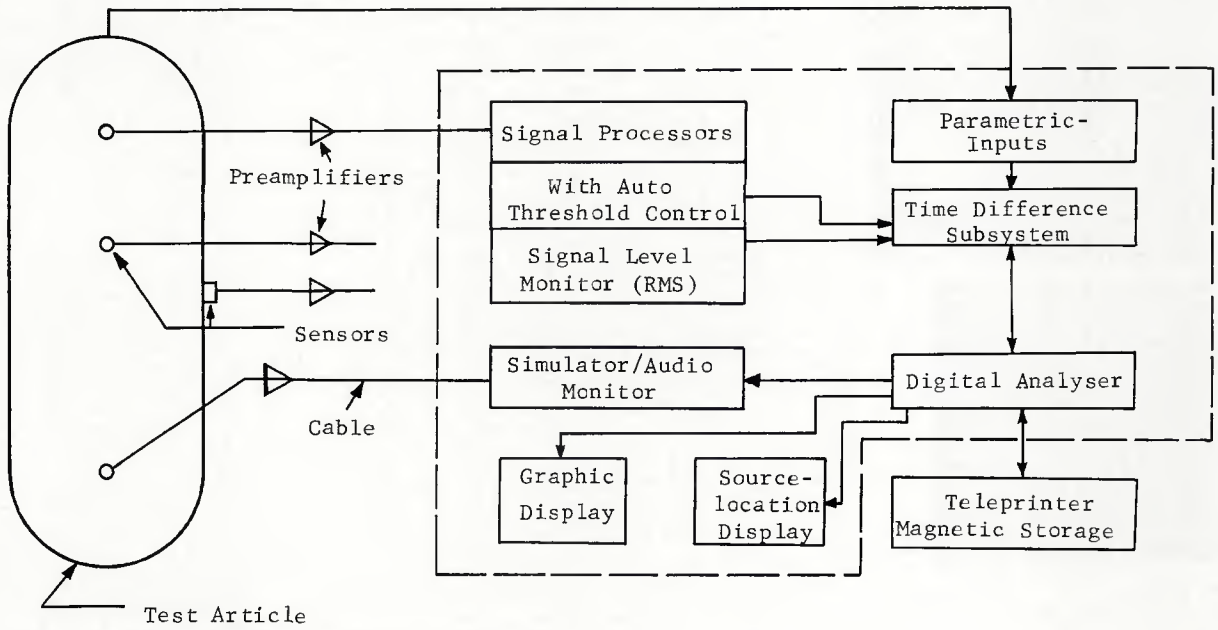

Fig. 9—Block diagram of the acoustic monitoring system

time for the weld to cool down to 125°C, i.e., 257°F (Fig. 4), the load was applied to the implant specimen and maintained until either rupture occurred or until it was judged that rupture would not take place (24 h). The ruptured specimen fracture surfaces were preserved by coating with Krylon® for fractographic examination discussed later. The specimens, which did not fail after 24 h, were cut out for further metallographic examination to

detect any cracks present.

Discussion of Results

The stress time-to-failure diagrams for the three heats examined at different hydrogen levels are shown in Figs. 5–7. Stresses were calculated based on the area at the root of the notch. In general, the lower critical stress decreased as the hydrogen level was increased in susceptible steels.

Figure 5 brings out the extreme susceptibility to HAC of heat 492S1871. Even when welding was done by the GMA process using (Ar + 2% O_2) mixture, the heat-affected zone (HAZ) showed a remarkable drop in stress-to-failure. It was presumed that small amounts of hydrogen must have been introduced into the heat-affected zone either from a hydrogen compound on the bare wire electrode or the test plate or from residual hydrogen in the steel, itself. Note that for these same conditions of welding, heat C10113 showed virtually no reduction in stress-to-failure (Fig. 6). Heat B259 (Fig. 7) showed no susceptibility to cracking at any hydrogen level examined. When loaded above the critical stress, failure in heat B259 occurred well away from the HAZ in the base metal after considerable plastic flow.

Figure 8 shows stress-to-failure diagrams for the three heats when welded with E7010 electrode. From Fig. 8 it can be seen that the lower critical stresses for cracking are in the same order as the susceptibilities to cold cracking in the slot weldability test (Table 3). The steel with the highest susceptibility to cracking in the slot test gave the lowest critical stress in the implant test. Hence, the results of the slot weld test correlated very well with those of the implant test.

Study of Initiation, Kinetics and Morphology of Hydrogen-Assisted Cracking

Acoustic emission (AE) techniques have been shown to have advantages over other methods in detecting small, discontinuous crack extensions such as in hydrogen embrittlement, stress corrosion cracking and fatigue processes (Ref. 27, 28). Studies of the kinetics of crack growth during hydrogen-assisted cracking employing AE techniques, particularly in welding, are scant (Ref. 29). In the referenced study (Ref. 29) no source location techniques were used, and very few details of the monitoring system are available. Moreover, testing was conducted on a very limited scale and only at low hydrogen concentrations.

In the present study, to provide additional information on the initiation and propagation of hydrogen-assisted cracking, AE monitoring technique was adopted by instrumenting the implant testing machine and also the slot weldability test sample after welding. A description of the AE system used and instrumentation of implant and slot weld test specimens follows.

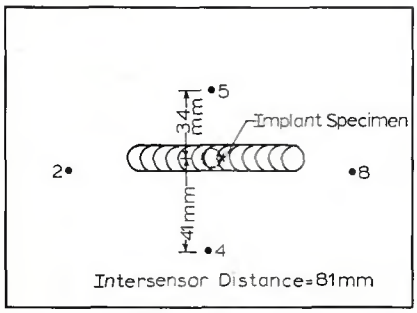

Fig. 10—AE sensor position on the base plate wth respect to weld and implant specimen

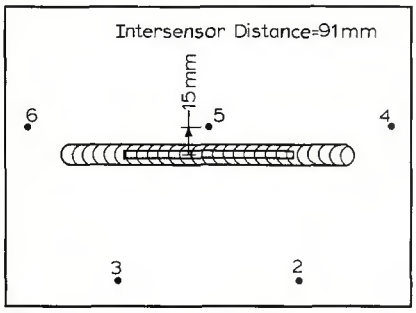

Fig. 11—AE sensor positions on slot weld test specimen

Investigatory Use of Acoustic Emission

General Description of the AE System

A block diagram of a 12-channel computerized AE system* is illustrated in Fig. 9. The system is designed for locating AE activity regions on a real time basis—that is, AE source location analysis and measurement of signal characteristics (amplitude, ringdown count and rms) are carried out and displayed on a CRT screen as they occur. The system also provides a complete record of the background noise levels during all portions of the test by means of a floating threshold, enabling the signal-to-noise ratio of the test to be continually established. Operation of the system is as follows.

Stress wave information from the test sample under consideration is picked up by piezoelectric sensors with a peak resonant frequency of 375 kHz nominal and a sensitivity greater than −75 dB referred to 1 volt (V) per microbar, operational in the temperature range from −250 to +200°C (−418 to +392°F). The sensors are 19 mm (¾ in.) in diameter and 22 mm (⅞ in.) high and are attached to the test piece by means of magnetic mounts. The sensors convert this mechanical stress wave to electrical signals sent by a length of transmission line to a preamplifier, which amplifies the low level AE signals and filters out extraneous noise. The signals are then processed in several ways. Signal level monitoring circuitry measures the rms output voltage levels, and AE detection is accomplished by discriminators or signal processors (gain continually adjustable from 0 to 60 dB and threshold adjustable from 10 mV to 10 V).

The discriminator pulses are used to define time differences for source location and for individual events when counting a total. The parametric data system transfers variable parameters of interest such as time, pressure, load, temperature, etc., into the monitoring system; this enables the system to present the AE data vs. the test parameter of interest.

For location of AE sources, the signal arrival time differences are processed by a minicomputer. The source locations are then plotted on a CRT display. Both source locations and event count data are stored on a digital cassette tape in a computer-reusable form.

The system also incorporates a simulator and an audio unit. The simulator unit is used to provide test pulses to AE sensors to check system operation and for source location calibration. The audio unit provides an output for audio perception of the AE activity. The audio output is useful to system users who can distinguish (with experience) crack noise and plastic deformation from mechanical and extraneous background noises.

Implant Tests

For the implant testing, sensor positions 2, 4, 5 and 8 of the 12 channels available were used to locate the sources of acoustic emission signals. The exact position of the center of the sensors on the base metal with respect to the weld and the implant are shown in Fig. 10. In order to secure the position of sensors on the base metal during testing (note that the sensors make contact with the welded side of the base metal, which is facing downwards during testing), the magnetic fixtures were glued to the backing plate at predetermined positions; the sensors were then placed face up in the hole in the magnet, the holes being just big enough to accomodate

Acoustic Emission Technology Corporation, Sacramento, California.

the sensors. A rubber cushion was provided between the magnet and the sensor so that some pressure would be exerted when the test plate was secured in place for testing. This ensured good contact between the test plate and the sensors. A copious amount of coupling agent (viz., silicone grease, Dow Corning 11® compound) was used to ensure good acoustical contact between test plate and sensors.

After welding with the conditions and procedures described previously, the slag and spatter were removed by chipping and the plate surface was cleaned by wire brushing. The test plate was then placed in position in the testing machine by dropping the plate onto the magnets (incorporating the sensors) and against the positioners, which made sure that the axis of the implant test piece and that of the loading arms were colinear. The base metal was then bolted onto the backing plate.

The entire procedure took approximately 90 seconds (s) to perform after welding. Load was applied to the implant specimens exactly 2 min after welding and acoustic emission monitoring was started the instant load was applied. Testing was conducted for both high hydrogen (welded with E7010) and low hydrogen (welded with E7018 electrode) conditions on heats C10113 and 492S1871 on only specific preselected stress levels as shown in Figs. 5 and 6. The stress levels were selected to represent the full range from below the critical stress to the highest, which had been determined previously.

Slot Weld Test

For the slot weldability test, sensor positions 2, 3, 4, 5 and 6 were used. The exact sensor positions on the test plate with respect to the weld are shown in Fig. 11. The positions of the sensors were pre-marked on the test plate.

After welding with the standard welding conditions, the plate was cleaned of spatter and slag on the top of the plate, and the slag on the bottom of the weld in the slot was also thoroughly removed. (Failure to remove the slag from the bottom of the weld in the slot resulted in an overwhelming amount of acoustic emissions, because the cracking in the plate and cracking of the slag apparently produce acoustic bursts of the same characteristics and frequency range so that the monitoring system has no way of distinguishing between the two. Hence, it was absolutely essential that slag from under the slot be removed).

Following cleaning, the sensors were placed in predetermined positions and secured in position by hold-down magnets. This entire procedure took about 140 s. Crack growth monitoring was started exactly 150 s after welding. The crack growth monitoring was done for heats C10113 and 492S1871 only for the high hydrogen (welded with E7010 electrode) condition, since it was previously determined that no cracking occurred in either of these heats when welded with E7018 electrode (low hydrogen).

For the acoustic emission monitoring studies on both implant tests and slot weldability tests, the following instrument settings were used: gain—70 dB; threshold—0.205 V; AE sensor used—Model AC 375-LM.

The threshold level was selected by trial and error. When a threshold of 0.8 V was used, only AE during the final fracture was registered and the rest of the signals were wiped out. A threshold of 0.41 V also resulted in a significant loss of emission data. A threshold of 0.150 V resulted in an enormous amount of spurious signals. A threshold level of 0.205 volts resulted in

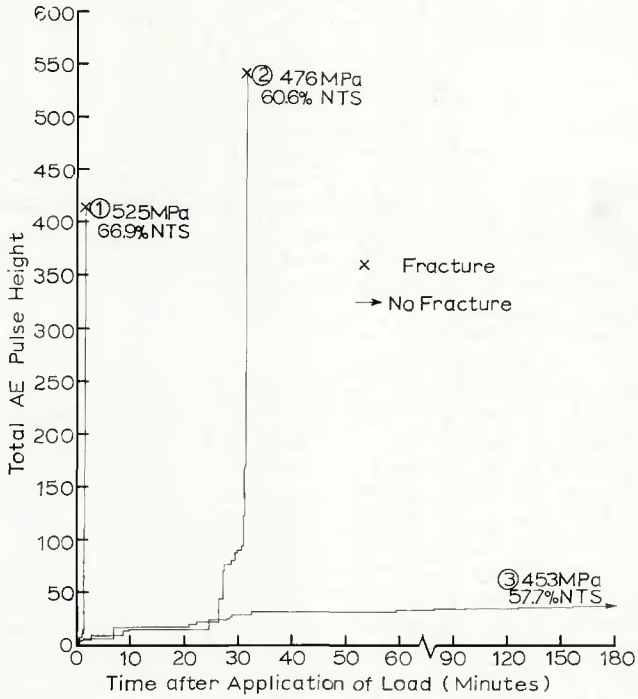

Fig. 12—Acoustic emission responses for implant tests in heat 492S1871 welded with E7010 at various stress levels

Fig. 13 (right)—Acoustic emission responses for implant tests in heat 492S1871 welded with E7018 at various stress levels

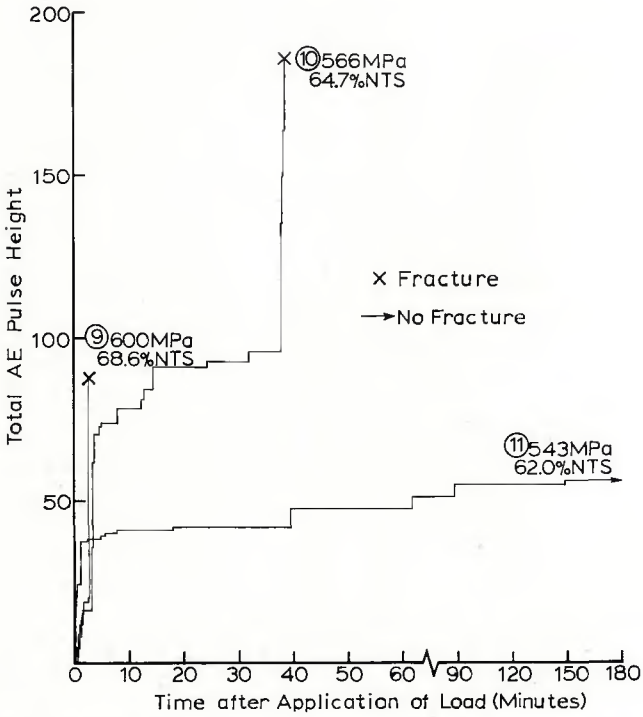

Fig. 14—Acoustic emission responses for implant tests in heat C10113 welded with E7010 at various stress levels

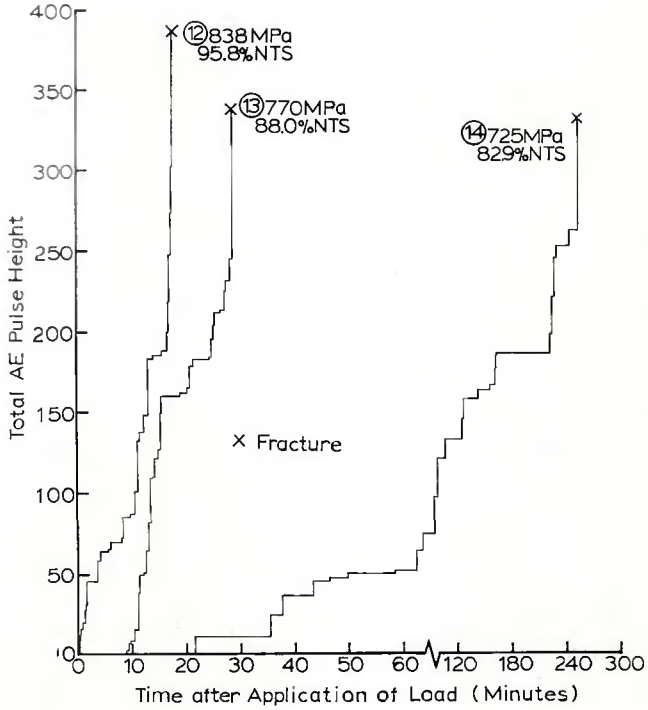

Fig. 15.—Acoustic emission responses for implant tests in heat C10113 welded with E7018 at various stress levels

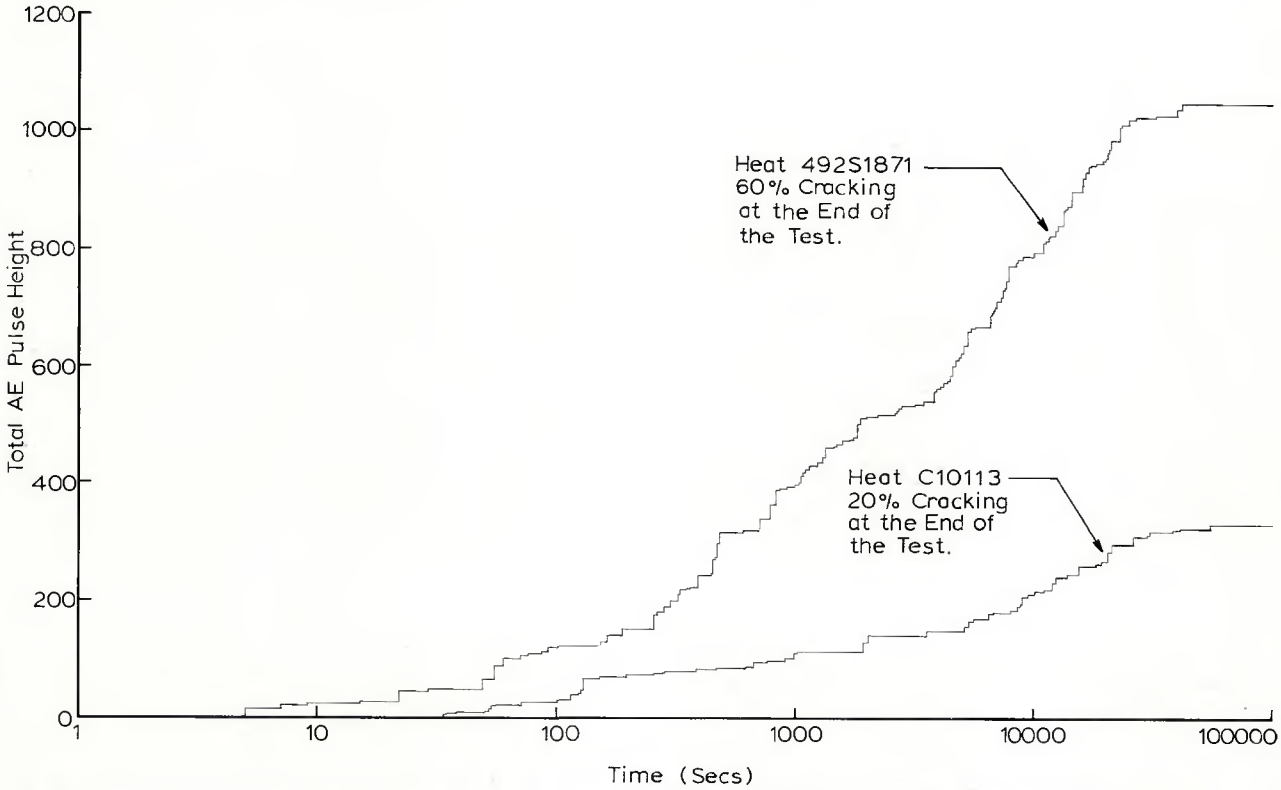

Fig. 16—Acoustic emission response in slot weld test for heats 492S1871 and C10113 welded with E7010 electrode

optimum operating conditions. Such low threshold levels are possible because in the present study a deadweight loading system was used.

If a hydraulic servo-controlled test system were to be used, more than an order of magnitude increase in threshold level would be required to eliminate background noise. The resulting loss of valuable emission data is readily apparent. In fact, Liptai *et al.* (Ref. 30) in an extensive review paper concluded that servo-hydraulic systems are almost unusable for acoustic emission analysis. This is particularly true where low amplitude acoustic signals are anticipated. This problem can be minimized, as in the present case, by using band pass filters.

Following testing, the fracture surfaces of both an implant and a slot weld test specimen (a 12 mm, i.e., 0.47 in., section was cut out at the center and broken open) were subjected to

fractographic study using the ETEC scanning electron microscope (SEM) operated in the secondary electron imaging mode at 20 kV.

Acoustic Emission Results

The results of acoustic emission studies conducted on heat 492S1871 and C10113 on both the implant and slot weldability tests are presented in Figs. 12 and 16 where cumulative total pulse height is plotted as a function of time. The specimen numbers denoted in Figs. 12 and 15 correspond to those in Figs. 5 and 6. Note that the stresses are also denoted as percent N.T.S. (notch tensile strength), which is taken as the stress at which the implant specimen would break within 10 s after loading when welded with GMA process using (Ar + 2% O_2) mixture as shielding gas. This makes possible the comparison of the two heats studied regarding crack growth rates.

A typical source location and total pulse height vs. time plot of events during a test as produced by CRT display are shown in Figs. 17 and 18, respectively. In Fig. 17, extraneous dots arising from stress wave reflections have been eliminated. Hence, the dots in Fig. 17 indicate the located positions of real acoustic emission sources and the dot concentration indicates the activity level and approximate position

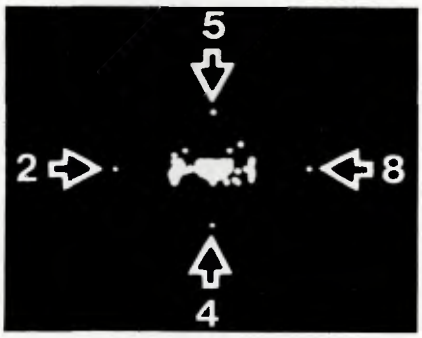

Fig. 17—Typical source location produced on CRT during implant test

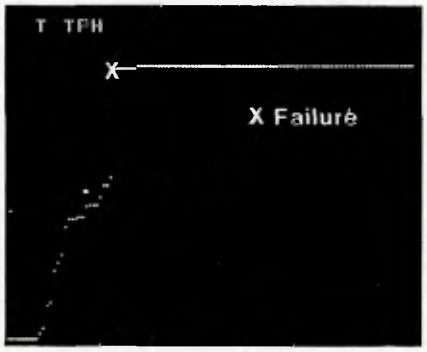

Fig. 18—Typical time vs. total pulse height plot on CRT screen during implant test. Full scale = 2 hours

of the source. The total pulse height vs. time plots given in Figs. 12 and 16 represent direct stress wave emissions coming from the sample.

With respect to initiation of cracking, it is seen from Figs. 12 and 13 that, in heat 492S1871 for all hydrogen concentration and stress levels examined, there was virtually no incubation time for crack initiation. The same behaviour was seen (Fig. 14) for heat C10113 at high hydrogen concentrations (welded with E7010 electrode). By contrast, in C10113 at low hydrogen concentrations produced by welding with E7018 electrodes, a definite incubation period was noted for crack initiation at lower stresses (Fig. 15). The lower the stress, the longer was the time for initiation of a crack.

The incubation period can be attributed to the time required for the critical hydrogen level to accumulate by diffusion to regions of triaxial stress just ahead of the notch (Ref. 17). The AE signals from the specimens were discrete events with a large range of amplitudes and pulse widths. In all cases, the high sensitivity of AE to the discontinuous nature of hydrogen-assisted cracking was evident. The quiet periods are probably the time required for sufficient hydrogen to diffuse to the crack tip.

In general, for all the conditions examined, the higher the stress, the faster was the crack growth rate and the shorter was the time for final fracture. Note also that the energy-to-

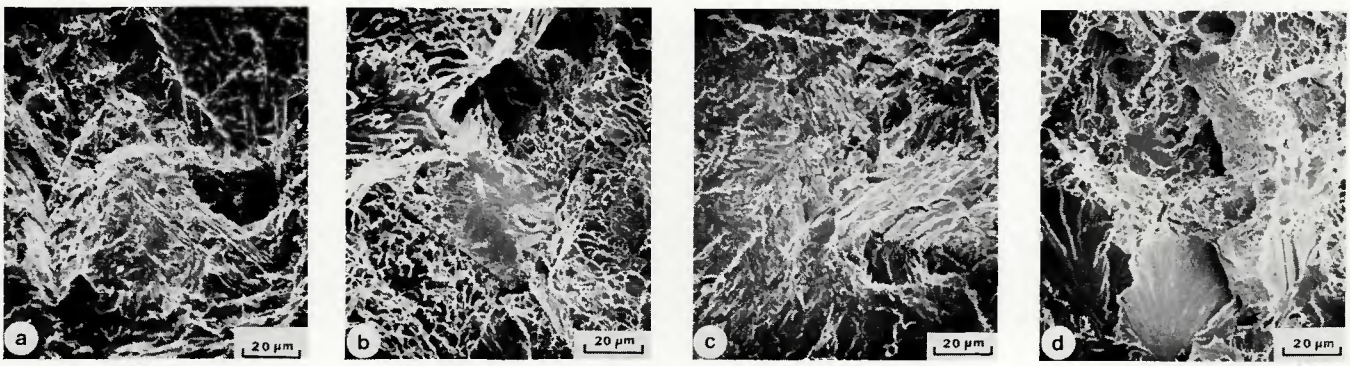

Fig. 19—Fracture morphology in implant test in heat 492S1871 welded with E7010 electrode: a—high stress, initiation site; b—high stress, near final failure; c—low stress, initiation site, d—near final failure. "a" corresponds to point 1 in Fig. 5; "c" corresponds to point 2 in Fig. 5.

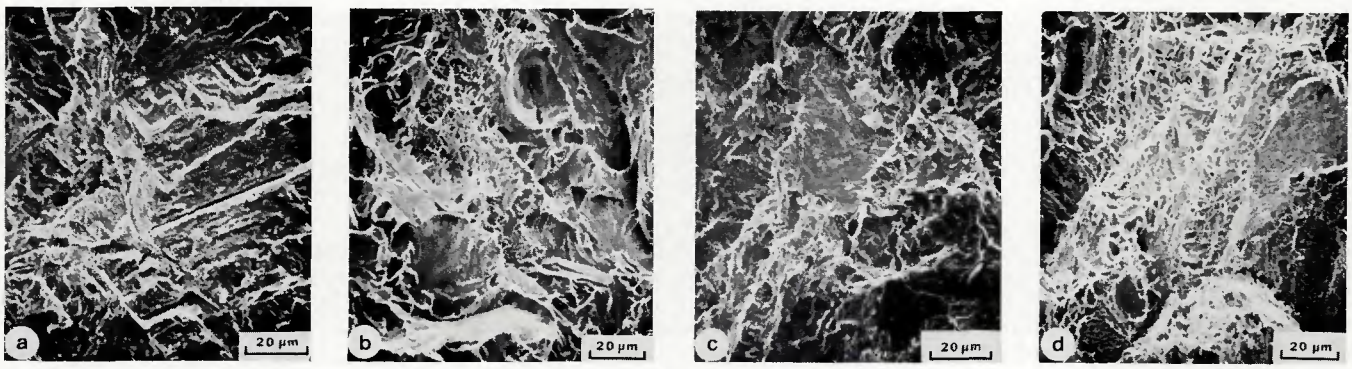

Fig. 20—Fracture morphology in implant test in heat 492S1871 welded with E7018 electrode: a—high stress, initiation site; b—high stress, close to failure; c—low stress, initiation site; d—low stress, close to final failure. "a" corresponds point 4 in Fig. 5, and "c" corresponds to point 6 in Fig. 5

failure (square of the pulse amplitude is proportional to energy) in heat C10113, in all cases, was significantly lower than that for heat 492S1871. From Figs. 12 and 16 it is also seen that the crack growth rates (for the same percent N.T.S. for implant specimens) in heat 492S1871 are faster than that in C10113. A possible explanation for these observations is given later based on fractographic information.

Fractographic Studies

Heat 492S1871

Figures 19 and 20 show the scanning electron microscopic (SEM) views of specific areas of the fracture surfaces in implant specimens of heat 492S1871 when welded with HYP E7010 electrode and E7018 electrode. The fracture mode at crack initiation was essentially transgranular quasi-cleavage (TGQC) with little contribution from intergranular (IG) failure.

As the crack propagated, the fracture morphology changed from one of quasi-cleavage (Figs. 19a, 19c, 20a, 20c) to one of TGQC associated with extensive microvoid coalescence (Figs. 19b, 19d, 20b, 20d). On the other hand, in specimens from the slot weldability test (Fig. 21), crack initiation was associated with microvoid coalescence (MVC) and TGQC, and the morphology changed entirely to quasi-cleavage associated with small amounts of IG failure.

Heat C10113

The fracture morphologies of implant specimens of heat C10113 welded with E7010 and E7018 electrodes are shown in Figs. 22 and 23, respectively. It is seen that the fracture mode at crack initiation was predominantly IG in nature. The amount of IG failure decreased with either an increase in initial stress (Figs. 23a, b and c) or with continued crack propagation giving way to TGQC (Figs. 22b–d), perfect cleavage (Fig. 23d) and TGQC associated with extensive MVC (Fig. 23b).

In the slot test also (Fig. 24), there was a small region of tear associated with MVC at the root of the notch (Fig. 24b) with the fracture mode changing immediately to QC (Fig. 24b) and further to QC and IG (Fig. 25c and d) as the crack propagated. Hence, in heat C0113 both IG and QC types of failure play an important role in hydrogen-induced cracking. This was in sharp contrast to heat 492S1871 in which fractographic study showed large areas of dimples and cleavage indicating that hydrogen-induced cracking occurred primarily by MVC and QC type of failure with very little contribution due to the IG process.

Discussion

Since hydrogen-induced cracking in steels is due to the combined action of hydrogen, stress and microstructure, the foregoing results can be explained in terms of these three factors.

Hydrogen and Stress

In welding, hydrogen available for the microcracking process is determined by the competing factors of hydrogen diffusion to the crack tip under a stress gradient and the escape of hydrogen from the weld metal to the atmosphere. This situation is depicted for both high and low hydrogen concentrations in the weld produced by E7010 and E7018 (properly dried) electrodes, respectively in Fig. 25.

It is assumed that, initially, the weld bead and the HAZ next to the fusion zone in the vicinity of the notch (where crack initiates) have a uniform distribution of hydrogen concentration of about 30 ppm in the case of the E7010 electrode and 5 ppm for the E7018 electrode. With the passage of time after welding, the average hydrogen concentration in the matrix (weld metal and coarse grain HAZ) will decrease due to the outgassing of the charged weld metal to the atmosphere and the surrounding base metal. The regions of high triaxial stress (near voids, just ahead of the notch or near internal cracks as dictated by the microstructure) in the coarse grain HAZ and weld metal have a high affinity for hydrogen, and the local concentration in this region becomes greater than that of the surrounding matrix. Thus, while the hydrogen concentration tends to increase in the regions of high triaxial stress, there is a decrease in the average hydrogen concentration in the matrix. This situation is depicted in Fig. 25b.

When the hydrogen concentration in the stressed region reaches a critical value (the higher the stress, the lower is the critical concentration of hydrogen necessary), either initiation of a crack or the extension of an existing crack takes place. In case of high initial hydrogen concentrations in the weld metal (E7010 electrode), little increase in local hydrogen concentration at stressed regions is necessary to cause cracking; whereas, for initially low hydrogen concentrations (E7018 electrode), depending on the stress level, considerable increase in hydrogen concentration must occur ahead of the crack tip (Fig. 25b).

As the crack propagates, part of the atomic hydrogen that had diffused into the triaxially stressed region is lost as molecular hydrogen behind the growing crack. This, together with the continual escape of hydrogen from the weld metal to the atmosphere with the passage of time, provides a situation wherein lesser and lesser amounts of hydrogen are available in the matrix for diffusion to the triaxially stressed regions.

Ultimately, the local hydrogen concentration at the crack tip will also decrease with time as shown in Fig. 25b. Finally, when the hydrogen concentration at the crack tip falls below the critical level for the existing local stress at the crack tip, further crack growth should cease. This is the situation for implant test specimens loaded below the lower critical stress as well as for slot weldability test specimens.

It is seen from Figs. 12 to 14 that, even when the specimens were loaded

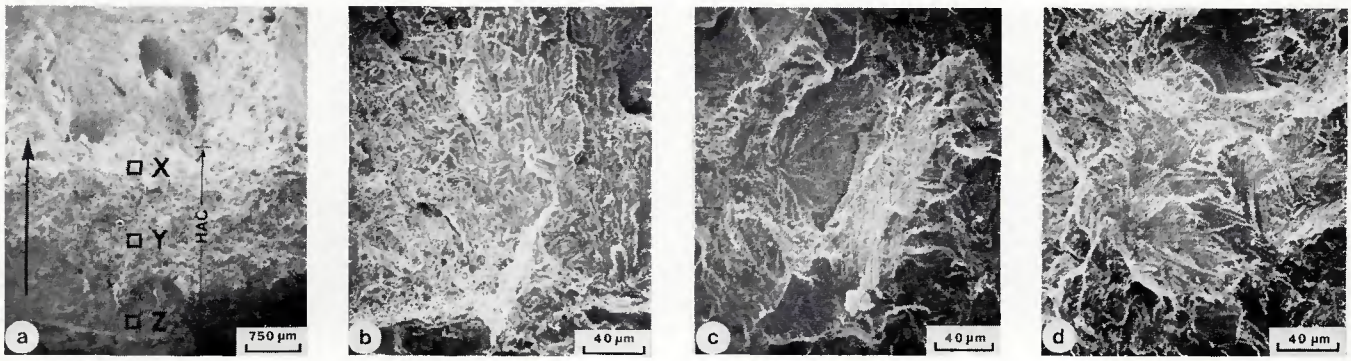

Fig. 21—Fracture morphology in slot weldability test in heat 492S1881 welded with E7010 electrode. a—center of weld in slot, general fracture appearance (arrow indicates direction of crack growth); b—position of Z in "a"; c—region Y in "a"; d—position X in "a"

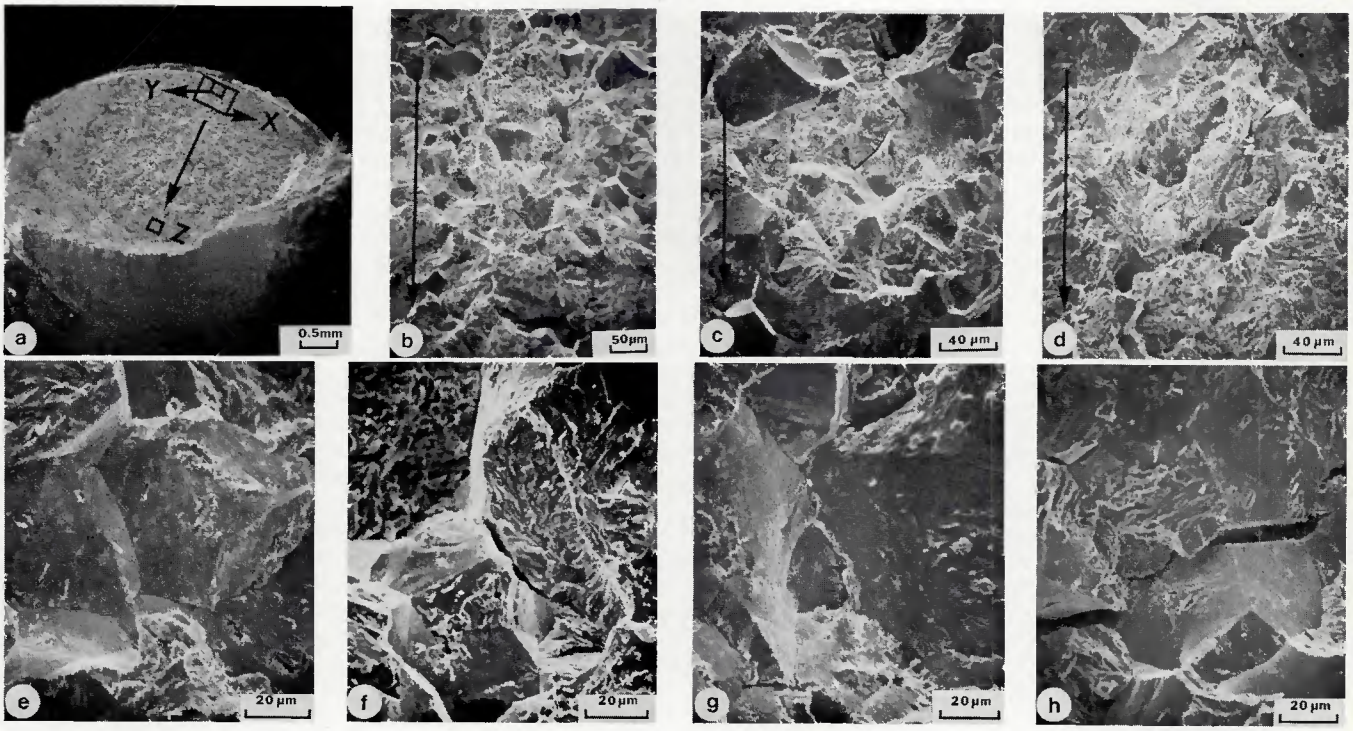

Fig. 22—General fracture surface and morphology in implant test in heat C10113 welded with E7010 electrode at low stress (point 10 in Fig. 6): a—general fracture surface in implant specimen (arrow indicates direction of crack growth); b—region X in "a"; c—region Y in "a" crack initiation site; d—region Z in "a," near final failure; e—high stress, initiation site; f—high stress, near final failure; g—low stress, initiation site; h—low stress, near final failure. "e" corresponds to point 8 in Fig. 6, and "g" corresponds to point 9A in Fig. 6

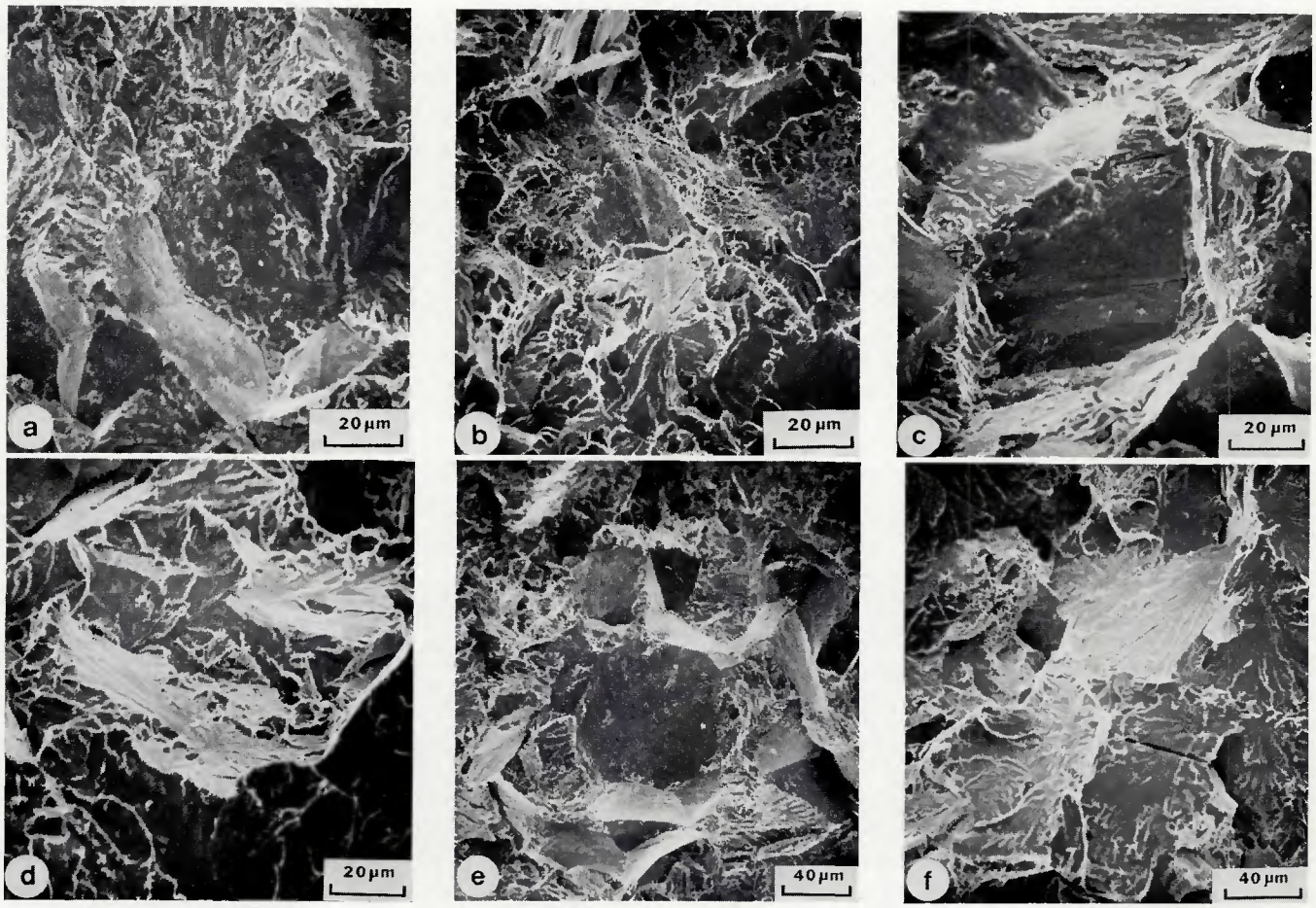

Fig. 23—Fracture morphology in implant test in C10113: a—high stress, initiation site; b—high stress, near final failure; c—intermediate stress, initiation site; d—intermediate stress, near final failure; e—low stress, initiation site; f—low stress, near final failure. "a" corresponds to point 12 in Fig. 6; "c" corresponds to point 13 in Fig. 6, and "f" corresponds to point 14 in implant test in Fig. 6

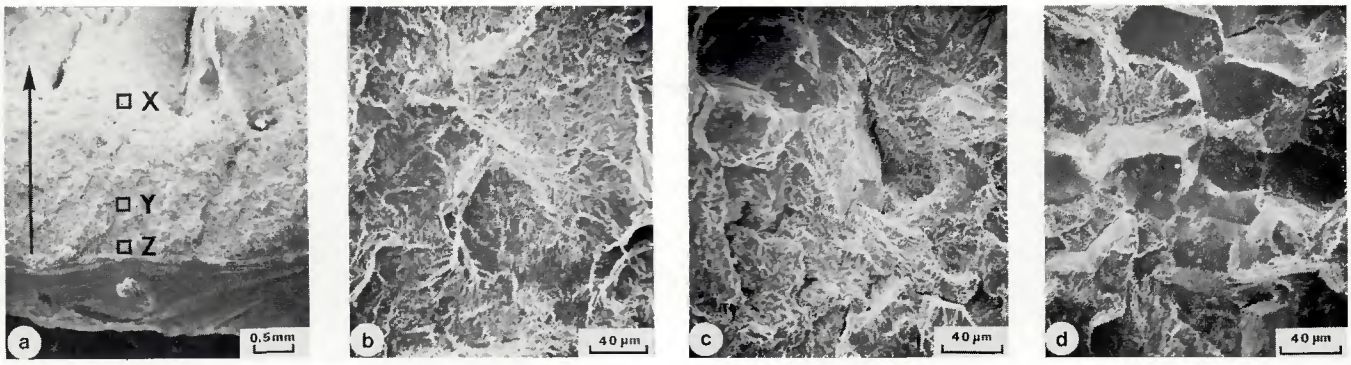

Fig. 24—Fracture morphology in slot weldability test in heat C10113 welded with E7010 electrode: a—center of weld, general fracture appearance (arrow indicates direction of crack growth); b—region Z in "a"; c—region Y in "a"; d—region X in "a," close to final fracture

below the critical stress, cracking started immediately upon loading. But the crack growth rate was slow enough so that the increase in stress intensity at the crack tip (as the crack the advanced could not keep pace with the decreasing concentration of hydrogen at the crack tip, and cracking eventally ceased.

The situation is slightly different in the slot weldability test. The test utilizes an internally restrained specimen. Hence, when a crack propagates, it produces a relaxation of the load. The fact that a change of fracture mode from one of MVC at crack initiation to QC and further to IG process was observed as the crack propagated in heat C10113 (Fig. 24) supports the view that the stress intensity at the crack tip decreases with continued crack propagation in the slot weldability test.

The situation is similar to a wedge-loaded specimen design (Ref. 19), which also produces a case of decreasing stress and a concomitant decreasing stress intensity as the crack grows. The decrease in stress intensity, together with the effusion of hydrogen, will cause eventual cessation of cracking (Fig. 25).

The need for accumulation of critical hydrogen concentration at the crack tip can also explain the quiet periods (Figs. 12–16) between increments of crack growth. Note that the lower the stress, the higher is the critical concentration of hydrogen necessary for crack growth and, hence, the longer are the quiet periods associated with longer periods of time for diffusion and build-up of hydrogen to the critical level. Every time a crack propagates, it leaves the site of critical hydrogen concentration. This process gives rise to the discontinuous nature of hydrogen-assisted cracking (Figs. 12–16).

With E7010 electrodes, the average concentration in the weld metal and coarse grain HAZ is so high (Fig. 25b) that it is probably well above the critical level at all stress levels examined in the implant test (Figs. 12 and 14) and in the slot weldability test (Fig. 16) for both heat 492S1871 and heat C10113. Hence, there is no need for an incubation period, and cracking is observed immediately upon loading.

In the case of the E7018 electrode, no incubation period was observed at all stress levels examined in heat 492S1871 (Fig. 13). In heat C10113 only the highest stress level registered no incubation period, while at lower stresses a definite incubation period was noted (Fig. 15). Of course, the lower the stress, the higher was the incubation period for crack initiation. This observation suggests that the critical hydrogen concentration necessary for crack initiation and growth in heat 492S1871 is very small (less than 5 ppm).

In heat C10113, the local hydrogen concentration at the crack tip will have to exceed the initial hydrogen concentration of 5 ppm (when welded with E7018) in the matrix at lower stress levels for crack initiation—hence the need for an incubation period in heat C10113 when welded with the E7018 electrode. This difference in behavior between the two steels is explained based on fractographic and microstructural features as follows.

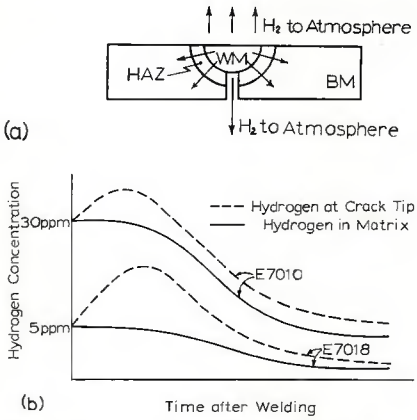

Fig. 25—Schematic showing diffusion tendencies of hydrogen in weldment: (a)—escape paths for hydrogen; (b)—variation of hydrogen concentration in the matrix and at the crack tip with time

Microstructure

Fractographic studies on fracture surfaces of the implant as well as the slot weldability tests indicated that, for all stress and hydrogen levels studied, the MVC and QC types were the major modes of failure in heat 492S1871; on the other hand, IG and QC types were the important modes of crack growth in heat C10113. To explain these observations, it is necessary to consider the microstructural features of the coarse grain HAZ in the two heats of steel (Figs. 26a and b). The HAZ microstructure of heat 492S1871 was untempered martensite, whereas that of C10113 was acicular low carbon martensite with autotempering during cooling.

It is not possible to define explicitly the exact form of martensitic (plate, lath or internally twinned etc.) structure seen in Fig. 26a. However, hydrogen-induced failure of lath or packet boundary (Ref. 6, 7, 31) and, hence, TGQC mode appears most reasonable in heat 492S1871. Both the hardness (Table 3) and grain size (Fig. 26a and b) of coarse grain HAZ in 492S1871 were higher than those of C10113. Hence, it is also possible that grain size and microstructure might be having synergistic effects.

Since the HAZ microstructure of heat 492S1871 was untempered martensite, it is possible that very high internal stresses were present within the microstructure, which was further augmented by the external stress. This might have led to a situation wherein, at all stress levels examined, the internal stresses were significantly higher (and, hence, lower critical concentration of hydrogen necessary for cracking). Thus, even when this heat of steel was welded with the E7018 electrode (low hydrogen), no incubation period was noted at all stress levels examined in implant testing.

Note that in heat C10113 the HAZ microstructure was low carbon martensite with autotempering. Autotempering reduced the internal stresses

within the microstructure in this heat of steel; consequently, higher external stresses and higher hydrogen concentrations were necessary for crack initiation growth. This could explain the need for an incubation period (for hydrogen diffusion to crack tip to attain critical concentration) in heat C10113 at lower applied external stresses when welded with the E7018 electrode. At the highest stress level examined, however, no initiation period was needed; this is probably because, at that stress level, the critical hydrogen concentration necessary for crack initiation was less than the hydrogen concentration in the matrix (about 5 ppm) at the instant of applying the load.

The very low hydrogen concentration necessary for cracking in heat 492S1871 was further evident from Fig. 5. Here there was a precipitous drop of stress-to-failure with time even when this steel was welded by GMA process using (Ar + 2% O_2) mixture. Note that C10113 showed virtually no reduction in stress-to-failure when welded under the same conditions, indicating higher hydrogen concentrations necessary for this steel to exhibit cracking.

It is clear from these results that the interaction between hydrogen and microstructure is very important in determining the initiation, the kinetics and the mode of the fracturing process.

Modeling and Mechanism for HAC

The relation between the stress intensity factor, hydrogen concentration at the crack tip, and the fracture mode for the two heats studied (i.e., 492S1871 and C10113) are summarized in Figs. 27a and 27b respectively. The stress intensity factors for implant specimens were calculated on the following assumptions:

1. Only the first unfused thread in the helical notch reacts to the load so that the effects of other threads can be neglected. It has been observed that tests conducted using both the helical notch and single circumferential notch have identical results for the lower critical stress in implant tests (Ref. 34).

2. Immediately after crack initiation, the situation can be approximated to the case of an infinitely sharp notch in a round bar (Fig. 28).

The stress intensity factors thus calculated have been plotted against hydrogen concentration at the crack tip in Figs. 27a and 27b. Note that the stress intensity factor values plotted in these figures are known quantitatively only at the instant of crack initiation (crossed points denoted by numbers)

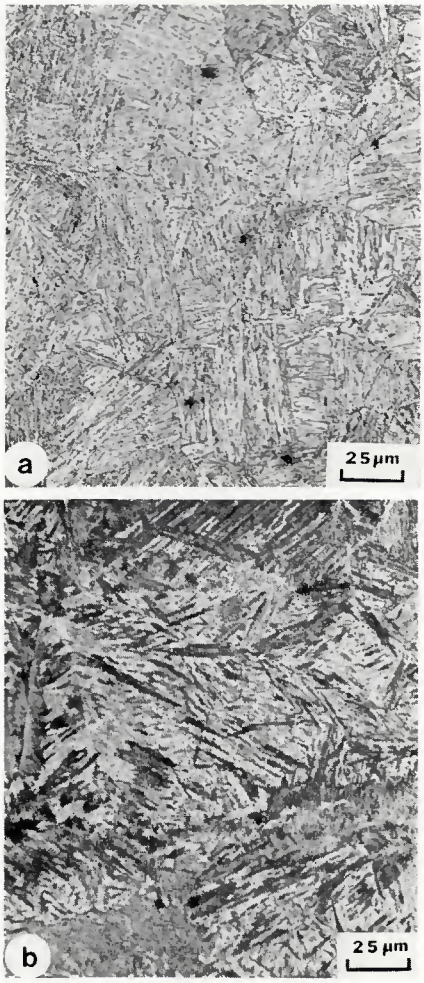

Fig. 26—Representative microstructures of coarse grain heat-affected zones of root passes in slot weld test: a—heat C10113; b—heat 492S1871. Nital etch

at the various stress levels studied in implant test.

The stress intensity factors provided during further crack propagation and that for the slot weldability test should be treated as being strictly qualitative (indicates trend only). Positions x and y on the abscissa correspond to concentration of hydrogen in the matrix 2 min after welding (instant of loading in the implant specimen) for E7018 and E7010 electrodes respectively. Note that this is equivalent to hydrogen concentration at the crack tip for cases where no incubation period for cracking is observed. In Fig. 27, it should be appreciated that the fracture process can be one of mixed modes along the leading edge of a crack if there is a change in the stress level and/or hydrogen concentration along the crack tip. No cracking would be expected below the lowest curve.

In general (for both Figs. 27a and 27b) at high stress intensities, the failure mechanism is MVC. At lower stress intensities concurrent with a small plastic zone size in which a large number of inclusions are not present, the fracture mode is one of QC. At still lower stress intensities the IG mode of failure, a process involving even less plastic deformation, occurs. It is also seen that increasing hydrogen concentration at the crack tip decreases the critical stress intensity at which these microfracture processes can occur. These findings are consistent with those of others (Ref. 19, 20, 29).

Acoustic emission studies showed (Figs. 12–15) the following:

1. The total pulse height-to-failure for heat 492S1871 was considerably higher than that for heat C10113.

2. The crack growth rates (for the same percent NTS) in heat 492S1871 were faster than those in C10113.

These observations can be rationalized by the fracture modes in these two steels. Since HAC in heat C10113 was shown to occur predominantly by IG mode (Figs. 22–24), it should be energetically the most favorable process (as supported by AE data), as it involves the least amount of plastic deformation compared to QC and MVC modes. It has been hypothesized that MVC and QC are relatively faster modes of fracture compared to IG mode (Ref. 18). Hence, higher crack growth rates should be expected in heat 492S1871, since QC and MVC were shown to be the dominant modes of failure (Figs. 19-21) in this steel.

The energetically favorable IG process is thought to be superceded at high stress intensities by the kinetically faster QC and MVC processes (Ref. 19).

For the case when the combination of stress intensity factor and hydrogen concentration at the crack tip corresponds to point 14 in Fig. 27b, the hydrogen concentration is insufficient to initiate crack growth at the instant the specimen is loaded. Hence, an incubation period is required so that sufficient hydrogen can diffuse to the crack tip.

When the hydrogen concentration reaches the level indicated by point A in Fig. 27b, cracking will initiate and grow and grow intergranularly for a short distance. As the crack grows, the stress intensity at the crack tip will increase, and the critical hydrogen concentration necessary for further growth of crack decreases. When the combination of stress intensity and hydrogen at the crack tip reaches point B, the mode of fracture changes to QC. The stress intensity will again increase until point C is reached where the fracture path assumes mixed mode. Ultimately, fracture occurs at point D.

Just below the lower critical stress, as represented by point 11 in Fig. 27b, cracking occurs immediately upon loading. But the rate of crack growth is

slow and the rate of hydrogen effusion is high enough to deplete the hydrogen level before the critical hydrogen level is reached at the crack tip for further crack growth as represented by point E in Fig. 27b. Thereafter, no further crack growth takes place. Such is the situation in slot weldability test specimens except, that in this test, the stress intensity factor decreases with crack growth as discussed before. This is shown by the dashed lines in Figs. 27a and b.

Finally, what significance do the results of the present study have to the potential mechanisms of hydrogen-assisted cracking? Fractographic observation of MVC, QC and IG processes are compatible with the suggestion by Beachem (Ref. 19, 20) that the presence of sufficiently concentrated hydrogen dissolved in the lattice just ahead of the crack tip lowers the stress required to drive whatever deformation processes the microstructure will allow.

Areas of "perfect cleavage" observed on some fracture surfaces (2d, 23f, 20b, 19d) also support the model that hydrogen reduces the binding energy between iron atoms and, therefore, the stress to propagate a crack (Ref. 17, 18). The interrelation between these two mechanisms and others (Ref. 13-16) is not very clear. However, what is quite clear is that hydrogen can strongly affect the yielding and flow characteristics of high-strength steels. Further, the present study demonstrates that hydrogen can react with microstructural features in quite different ways. Moreover, this interaction can strongly affect the kinetics and morphology of crack growth in steels.

Summary

The results of this investigation may be summarized as follows:

1. The lower critical stess in the implant test ranked the steels in the same order of their susceptibility to hydrogen-assisted cracking as did the slot weld test, indicating a close correlation between the two tests.

2. Acoustic emission studies showed that crack initiation in heat 492S1871 occurred immediately after loading at all stress and hydrogen levels examined. However, heat C10113 showed no incubation period at high hydrogen levels and a definite incubation period for crack initiation at lower stress levels and low hydrogen concentrations. The lower the stress, the longer was the incubation period.

3. Crack growth rates in heat 492S1871 were higher than in heat C10113 in both implant and slot weldability test specimens.

4. Fractographic studies revealed that crack propagation in heat C10113 was predominantly intergranular; whereas crack propagation in heat 492S1871 occurred by quasi-cleavage and microvoid coalescence, both being relatively rapid fracture processes.

5. Hydrogen-assisted cracking is very sensitive to microstructural features and this interaction can dictate the kinetics and morphology of crack growth.

6. The results of this study are compatible both with Beachem's model for HAC and with the lattice decohesion theory. The interrelation between these two theories is not very clear.

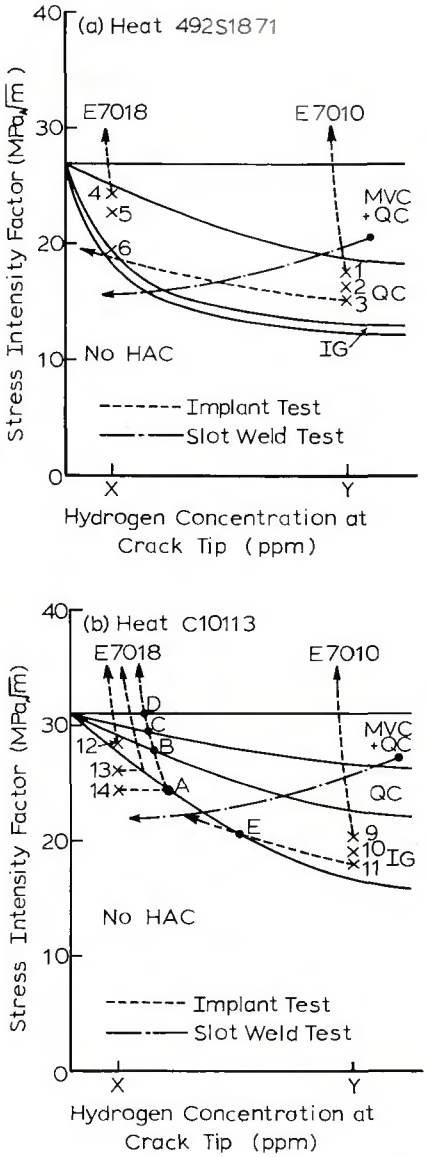

Fig. 27—Schematics showing the combined effects of stress intensity and hydrogen concentration at the crack tip on the mode of fracture: Top—heat 492S1871; bottom—heat C10113

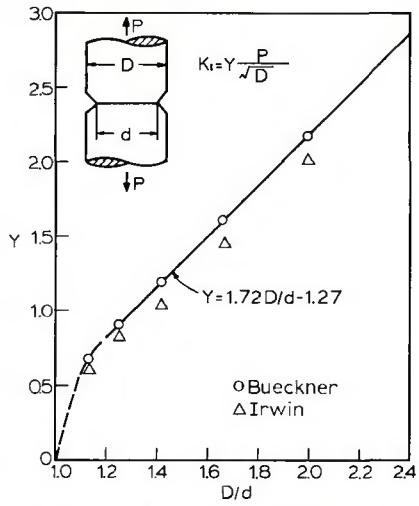

Fig. 28—Stress intensity factor solution for a round bar with a notch (Ref. 131)

Acknowledgment

The authors would like to acknowledge the help rendered by Mr. G. V. Krishna of Air Products and Chemicals, Inc. in conducting acoustic emission studies.

This investigation was supported by The American Iron and Steel Institute and guided by the Weldability Committee of the Welding Research Council. The authors are grateful for their support and assistance.

References

1. Vasudevan, R.; Stout, R. D.; and Pense, A. W. 1980. A field weldability test for pipeline steels—Part II. *Welding Journal* 59(3): 76-s to 86-s.

2. Boniszewski, T. and Watkinson, F. 1973. Effect of weld microstructures on hydrogen-induced cracking in transformable steels—Parts I and II. *Metals and Materials* Feb., 90-96, March, 145-151.

3. Boniszewski, T.; Watkinson, F.; Baker, R. G.; and Tremlett, H. F. 1965. Hydrogen embrittlement and heat-affected zone cracking in low carbon alloy steels with acicular microstructures. *British Welding Journal* 12(7): 14-36.

4. Boniszewski, T. and Baker, R. G. 1965. Hydrogen Embrittlement in Low Carbon Nickel and Manganese Steels. *British Welding Journal* 12(7): 349-362.

5. Wayman, M. L. and Smith G. C. 1970. The hydrogen embrittlement of Fe-Ni martensites. *Met Trans* (1): 1189.

6. Bernstein, I. M. 1970. Hydrogen-induced cracking in iron: morphology and crack path dependence. *Met Trans* (1): 3143.

7. Bernstein, I. M. 1970. The role of hydrogen in the embrittlement of iron and steel. *Matls. Sci. Eng.* 6: 1.

8. Evans, G. M. Correlation of the C.T.S. test with the implant test. IIW, Doc. II-A-292-71 and IX-814-72.

9. Satoh, K. *et al.* Correlation of the implant test with the PRC and TRC tests. IIW Doc. IX-874-74.

10. Watanabe, K. *et al.* Studies of delayed crack in welds of high-strength steel. IIW Doc. No. IX-920-75.

11. Kirihara, S.; Onuma, T.; Watanabe, K.; and Satoh, K. Studies of delayed crack in welds of high-strength steel-correlation of

method of various weld cracking. IIW, Doc. No. IX-956-76.

12. Horikawa, K.; Akazawa, J.; Matsui, 5.; and Ohkuma, Y. Correlation of various weld cracking tests. IIW, Doc. IX-966-76.

13. Zapfee, C. A. and Sims, C. E. 1941. Hydrogen embrittlement-internal stress and defects in steel. *Trans. AIME* (145): 225.

14. Tetelman, A. S. 1969. The mechanism of hydrogen embrittlement in steel. *Proc. Fund. Aspects of Stress Corrosion Cracking* p. 446. Houston, Texas: NACE.

15. Petch, N. J. 1956. The lowering of fracture stress due to surface adsorption. *Phil. Mag.* (1): 331-337.

16. Petch, N. J. and Stables, P. 1952. Delayed fracture of metals under static load. *Nature* 169: 842.

17. Troiano, A. R. 1960. The role of hydrogen and other intersticials in the mechanical behavior of metals. *Trans. ASM* 52(1): 54-80.

18. Oriani, R. A. and Josephic, W. 1972. Testing of the decohesion theory of hydrogen-induced crack propagation. *Scripta Met* (6): 681.

19. Beachem, C. D. 1972. The new model for hydrogen-assisted cracking (hydrogen "embrittlement"). *Met. Trans.* 3(2): 437-451.

20. Beachem, C. D. 1977. Electron fractographic support for a new model for hydrogen-assisted cracking. Proc. Confce. on *Stress Corrosion Cracking and Hydrogen Embrittlement of Iron Base Alloys:* Houston, Texas: NACE.

21. Savage, W. F.; Nippes, E. F.; and Homma, H. 1976. Hydrogen induced cracking in HY-80 steel weldments. *Welding Journal* 55(11): 368-s to 365-s.

22. Savage, W. F.; Nippes, E. F.; and Tokunaga, Y. 1978. Hydrogen induced cracking in HY-130 steel weldments. *Welding Journal* 57(4): 118-s to 126-s.

23. Stout, R. D.; Vasudevan, R.; and Pense, A. W. 1976. A field weldability test for pipeline steels. *Welding Journal* 55(4): 89-s to 94-s.

24. Vasudevan, R. 1979. Field weldability and hydrogen-assisted cracking in H5LA pipeline steels including the arctic grade. Ph.D. Dissertation, Dept. of Metallurgy and Materials Eng. Lehigh University.

25. Granjon, H. 1969. The implant method for studying the weldability of high strength steels. *Metal Construction and British Welding Journal* 1(2): 112.

26. Sawhill, Jr., J. M.; Dix, A. W.; and Savage, W. F. 1974. Modified implant test for studying delayed cracking. *Welding Journal* 53(12): 554-s to 559-s.

27. Hartbower, C. E.; Gerberich, W. W.; and Crimmins, P. P. 1968. Monitoring subcritical crack growth by detection of elastic stress waves. *Welding Journal* 47(1): 1-s to 18-s.

28. Dunegan, H. L. and Tetelman, A. S. 1976. Non-destructive characterization of hydrogen embrittlement cracking by acoustic emission techniques. *Eng. Fr. Mech.* 2: 387-402.

29. Savage, W. F.; Nippes, E. F.; and Sawhill, Jr., J. M. 1976. Hydrogen-induced cracking during implant testing of alloy steels. *Welding Journal* 55(12): 400-s to 407-s.

30. Liptai, R. G.; Harris, D. O.; Engle, R. B.; and Tatro, C. A. 1971. Acoustic emission techniques in materials research. *International Journal of Non-Destructive Testing* 3: 215-275.

31. Rath, B. B. and Bernstein, I. M. The relation between grain boundary orientation and intergranular cracking. *Met Trans* (2): 2845.

32. Christensen, N. Weldability testing by the implant method. I.I.W. Doc. IX-824-73.

33. Brown, Jr., W. F. and Srawley, J. E. 1966. ASTM, STP 410.